



Published in final edited form as:

*Biomater Sci.* ; 9(21): 7134–7150. doi:10.1039/d1bm01113h.

## The *in vivo* fate of tobacco mosaic virus nanoparticles theranostic agents modified by the addition of a polydopamine coat

Christian Isalomboto Nkanga<sup>1</sup>, Young Hun Chung<sup>2</sup>, Sourabh Shukla<sup>1</sup>, Jingcheng Zhou<sup>1</sup>,  
Jesse V. Jokerst<sup>1,3,4</sup>, Nicole F. Steinmetz<sup>1,2,4,5,6,7,\*</sup>

<sup>1</sup>Department of NanoEngineering, University of California San Diego, 9500 Gilman Dr., La Jolla  
CA 92039, United States

<sup>2</sup>Department of Bioengineering, University of California San Diego, 9500 Gilman Dr., La Jolla CA  
92039, United States

<sup>3</sup>Materials Science and Engineering Program, University of California San Diego, 9500 Gilman  
Dr., La Jolla CA 92039, United States

<sup>4</sup>Department of Radiology, University of California San Diego, 9500 Gilman Dr., La Jolla CA  
92039, United States

<sup>5</sup>Center for Nano-ImmunoEngineering, University of California San Diego, 9500 Gilman Dr., La  
Jolla CA 92039, United States

<sup>6</sup>Moore's Cancer Center, University of California San Diego, 9500 Gilman Dr., La Jolla CA 92039,  
United States

<sup>7</sup>Institute for Materials Discovery and Design, University of California San Diego, 9500 Gilman Dr.,  
La Jolla CA 92039, United States

### Abstract

Plant virus nanoparticles (VNPs) have multiple advantages over their synthetic counterparts including the cost-effective large-scale manufacturing of uniform particles that are easy to functionalize. Tobacco mosaic virus (TMV) is one of the most promising VNP scaffolds, reflecting its high aspect ratio and ability to carry and/or display multivalent therapeutic ligands and contrast agents. Here we investigated the circulation, protein corona, immunogenicity, and organ distribution/clearance of TMV particles internally co-labeled with cyanine 5 (Cy5) and chelated gadolinium (Gd) for dual tracking by fluorescence imaging and optical emission spectrometry, with or without an external coating of polydopamine (PDA) to confer photothermal and photoacoustic capabilities. The PDA-coated particles (Gd-Cy5-TMV-PDA) showed shorter plasma circulation time and broader distribution to organs of the reticuloendothelial system (liver, lungs, and spleen) than uncoated Gd-Cy5-TMV particles (liver and spleen only). The

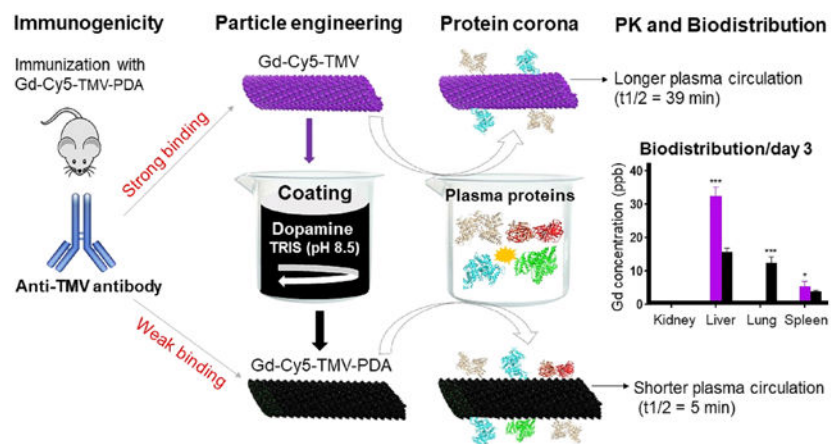
\*Corresponding author: nsteinmetz@ucsd.edu.

Declaration of competing interest

Dr. Steinmetz is a co-founder of and has a financial interest in Mosaic ImmunoEngineering Inc. The other authors declare no potential conflict of interest.

Gd-Cy5-TMV-PDA particles were surrounded by 2–10-fold greater protein corona (containing mainly immunoglobulins) compared to Gd-Cy5-TMV particles. However, the enzyme-linked immunosorbent assay (ELISA) revealed that PDA-coated particles bind 2-fold lesser to anti-TMV antibodies elicited by particle injection than uncoated particles, suggesting that the PDA coat enables evasion from systemic antibody surveillance. Gd-Cy5-TMV-PDA particles were cleared from organs after 8 days compared to 5 days for the uncoated particles. The slower tissue clearance of the coated particles makes them ideal for theranostic applications by facilitating sustained local delivery in addition to multimodal imaging and photothermal capabilities. We have demonstrated the potential of PDA-coated proteinaceous nanoparticles for multiple biomedical applications.

## Graphical Abstract



## Keywords

Plant virus; tobacco mosaic virus; gadolinium; polydopamine; nanoparticles biodistribution and clearance; photoacoustic imaging

## INTRODUCTION

Biomedical imaging is facilitated by contrast agents that enhance the visibility of anatomical structures, enabling clinicians to distinguish lesions from healthy tissue. Paramagnetic ions such as gadolinium ( $\text{Gd}^{3+}$ ) are used as contrast agents in magnetic resonance imaging (MRI), and they work by affecting the relaxation rate ( $R_1 = 1/T_1$ ) of the surrounding water protons.<sup>1</sup> Numerous Gd-based contrast agents have been approved for clinical use,<sup>2</sup> but small-molecule contrast enhancers achieve a lower sensitivity than predicted by theory.<sup>3</sup> Theoretically, one  $\text{Gd}^{3+}$  ion should enhance relaxivity by  $80\text{--}100 \text{ mM}^{-1} \text{ s}^{-1}$  in a clinical-strength magnetic field (1.5 T) but in practice the typical relaxivity is only  $3\text{--}5 \text{ mM}^{-1} \text{ s}^{-1}$  per  $\text{Gd}^{3+}$  ion.<sup>4</sup> This partly reflects the rapid molecular tumbling and low hydration states of approved  $\text{Gd}^{3+}$  complexes, increasing the dosage requirement to  $\sim 15 \text{ mg kg}^{-1}$  body weight and thus raising safety concerns,<sup>5,6</sup> as well as restricting applications when high concentrations are needed for enhanced local contrast.<sup>7-9</sup>

The engineering of nanoscale materials has facilitated the development of functional nanoparticles (NPs) suitable for various biomedical applications, such as drug delivery, gene therapy, immunotherapy, and diagnosis.<sup>10</sup> The diagnostic potential of NPs reflects their use for noninvasive imaging, which is facilitated by the ability to engineer the size, shape and surface properties of particles to achieve the site-specific delivery and accumulation of imaging agents.<sup>11</sup> Gd-loaded NPs reduce the tumbling rate and improve sensitivity compared to Gd<sup>3+</sup> complexes by increasing the local concentrations of Gd<sup>3+</sup> at the target site, enhancing the total molar relaxivity and signal intensity.<sup>7,12</sup> Accordingly, paramagnetic Gd-based nanocrystals achieved ultrahigh relaxivity of  $\sim 80 \text{ mM}^{-1} \text{ s}^{-1}$  per Gd<sup>3+</sup> at 1.41 T, approximately 25-fold higher than typical Gd<sup>3+</sup> complexes.<sup>13</sup> However, despite the clinical advantages of nanoscale contrast enhancers, only a few have been approved and most of these are based on iron oxide. For example, Ferumoxtran-10 Combidex Sinerem and Feridex I V Endorem are dextran-coated iron oxide NPs used to image lymph node metastases and liver lesions, respectively.<sup>14</sup> The successful clinical development of nanoscale imaging agents is hindered by batch-to-batch variation and scale-up issues during synthesis as well as challenges with selective targeting, biocompatibility, and toxicity inherent to synthetic NPs.<sup>15</sup>

Plant virus nanoparticles (VNPs) can overcome the disadvantages of synthetic particles because they have a genetically encoded uniform structure, allowing cost-effective manufacturing in plants with batch-to-batch reproducibility.<sup>16</sup> VNPs achieve good biocompatibility because they are non-toxic, biodegradable and do not infect mammalian cells,<sup>17</sup> making them a safe platform technology for the delivery of contrast agents,<sup>18,19</sup> including Gd<sup>3+</sup> complexes.<sup>20-22</sup> One of the most versatile VNP scaffolds is tobacco mosaic virus (TMV), which features 2130 identical coat protein subunits that form  $300 \times 18 \text{ nm}$  rods with a 4-nm internal channel, allowing both internal and external modifications by conjugation or genetic engineering. The high aspect ratio of TMV helps it evade the immune system while achieving efficient margination toward blood vessel walls, which enhances endothelial targeting and increases the possibility of interactions between the molecular target and the imaging probe.<sup>23</sup> We previously showed that the conjugation of Gd(DOTA) to TMV leads to a remarkable increase in ionic relaxivity from  $4.9 \text{ mM}^{-1} \text{ s}^{-1}$  for plain Gd(DOTA) to  $18.4 \text{ mM}^{-1} \text{ s}^{-1}$  for the TMV formulations at 60 MHz.<sup>24</sup> The utility of these TMV-based MR contrast agents was demonstrated in imaging studies in a mouse model of atherosclerosis: the loading of Gd(DOTA) complexes in TMV particles allowed for detection and imaging of atherosclerotic plaques at 400-folds reduced dose.<sup>25</sup> More recently, we coated Gd(DOTA)-conjugated TMV with polydopamine (PDA),<sup>26</sup> a mussel-inspired polymer with photothermal properties.<sup>27,28</sup> The PDA coating significantly increased the relaxivity of Gd(DOTA)-conjugated TMV at 60 MHz:  $\sim 80 \text{ mM}^{-1} \text{ s}^{-1}$  for PDA-coated particles compared to  $13.63 \text{ mM}^{-1} \text{ s}^{-1}$  for uncoated particles.<sup>26</sup> The PDA-coated Gd(DOTA)-loaded TMV particles also achieved the effective photothermal killing of PC-3 prostate cancer cells as well as high photoacoustic contrast. In another study, Lemaster et al. demonstrated that the loading of Gd<sup>3+</sup> ions in PDA-based NPs leads to 40-fold enhancement in photoacoustic signal intensity relative to PDA-based NPs alone.<sup>29</sup> These combined characteristics make the Gd-TMV-PDA system a promising theranostic formulation capable of multimodal MRI and photoacoustic imaging to guide photothermal therapy.

In order to advance PDA-coated Gd(DOTA)-loaded TMV particles to the clinic, it is necessary to determine their *in vivo* fate. We therefore investigated the plasma circulation, biodistribution and clearance of these particles, and determined their potential interactions with plasma proteins and anti-TMV antibodies. We labeled Gd-TMV-PDA particles with fluorophore Cyanine 5 (sulfo-Cy5) to facilitate tracking using different modalities (i.e., detection of Gd<sup>3+</sup>, sulfo-Cy5 and PDA), and to test the capacity of the particles for additional functionalization.

## EXPERIMENTAL SECTION

### Particles manufacturing and characterization

**TMV preparation.**—Wild-type TMV was propagated in and purified from *Nicotiana benthamiana* plants as previously described.<sup>30</sup> Briefly, frozen infected leaves were homogenized in 0.1 M potassium phosphate (KP) buffer containing 0.2% (v/v) 2-mercaptoethanol (Thermo Fisher Scientific), filtered through two layers of cheesecloth, and centrifuged (11,000 × g, 4°C, 20 min) to remove plant materials. The supernatant was mixed with 1:1 (v/v) chloroform:butanol-1 and the aqueous phase was transferred to 0.2 M NaCl and 8% polyethylene glycol (PEG) 8000 (Thermo Fisher Scientific) to precipitate the VNPs. Following resuspension and removal of pelleted polymer aggregates, TMV particles were purified by ultracentrifugation on a 40% (w/v) sucrose cushion (160,000 × g, 4°C, 3h). The concentration of TMV was measured on a NanoDrop 2000 spectrophotometer (Thermo Fisher Scientific).

**Synthesis of Gd-Cy5-TMV.**—TMV particles were internally decorated with alkyne handles, then conjugated to Gd(DOTA)-azide and sulfo-Cy5-azide using copper-mediated azide–alkyne cycloaddition (CuAAC, also called click chemistry) as previously described.<sup>23</sup> Briefly, the alkynes were grafted by mixing 2 mL of TMV (10 mg/mL in 0.01 M KP buffer) with 5.74 mL 0.1 M HEPES (pH 7.4), 1.3 mL 0.1 M propargylamine and 30 mg hydroxybenzotriazole (Sigma-Aldrich). The reaction was stirred at room temperature before adding 0.32 mL of 0.1 M aqueous *N*-(3-dimethylaminopropyl)-*N'*-ethylcarbodiimide (EDC, Sigma-Aldrich) at 0, 6 and 18 h. Following complete EDC addition, the reaction was stirred for another 24 h. The alkyne-labeled TMV was purified by ultracentrifugation on a 40% (w/v) sucrose cushion (160,000 × g, 4 °C, 3 h).

For the click reaction, 0.056 mL of 0.1 M Gd(DOTA)-azide and 0.02 mL of 0.01 M sulfo-Cy5-azide (Lumiprobe) were added to 9 mL of alkyne-labeled TMV (2.2 mg mL<sup>-1</sup> in 0.01 M KP buffer) followed by the addition of 0.1 mL of 0.2 M aminoguanidine, 0.1 mL of 0.2 M sodium ascorbate and 0.1 mL of 0.1 M CuSO<sub>4</sub> (Acros Organics). The mixture was stirred for 30 min before stopping the reaction with 0.1 mL of 0.5 M EDTA (Sigma-Aldrich). The resulting Gd-Cy5-TMV particles were purified by ultracentrifugation on a 40% (w/v) sucrose cushion (133,000 × g, 4 °C, 1 h). The loading of sulfo-Cy5 and Gd<sup>3+</sup> were confirmed by UV-Vis spectrometry and inductively coupled plasma optical emission spectrometry (ICP-OES), respectively; the latter was accomplished using a 730-ES device (Agilent Technologies). Particle integrity was confirmed by size exclusion chromatography (SEC) using a Superose6 column on the ÄKTA Explorer chromatography system (GE

Healthcare). The TMV coat protein, genomic RNA and sulfo-Cy5 were detected at 260, 280 and 647 nm, respectively.

**Preparation of Gd-Cy5-TMV-PDA.**—We added 12 mg dopamine (Sigma-Aldrich) to 8 mg Gd-Cy5-TMV in 80 mL Tris buffer (pH 8.5), stirred at room temperature for 6 h, pelleted the particles by centrifugation ( $25,000 \times g$ , 4 °C, 20 min) and washed them in phosphate-buffered saline (PBS) and Millipore water.<sup>26</sup> Wild-type TMV particles were coated under the same conditions to produce a TMV-PDA control alternative to blank PDA (also produced using the same protocol). Coating was assessed by electron microscopy prior to further characterization by photothermal and photoacoustic analysis.

**Sodium dodecylsulfate polyacrylamide gel electrophoresis (SDS-PAGE).**—

Wild-type and modified TMV particles were analyzed by SDS-PAGE as previously described.<sup>31</sup> Samples were mixed with the loading buffer (62.5 mM Tris-HCl pH 6.8, 2% (w/v) SDS, 10% (v/v) glycerol, 0.01% (w/v) bromophenol blue, 10% (v/v) 2-mercaptoethanol) and heated for 5 min at 100 °C for denaturation. Denatured samples were separated on 4–12% or 12% NuPAGE polyacrylamide gels in 1× (3-(*N*-morpholino) propanesulfonic acid) running buffer (MOPS, Invitrogen) at 200 V for 40 min alongside SeeBlue Plus2 pre-stained protein standards (Thermo Fisher Scientific). An AlphaImager system (Protein Simple) was used to image the gels under red and white light before staining with Coomassie Brilliant Blue. The gels were imaged again under white light after staining.

**Transmission electron microscopy (TEM).**—Samples (10 µL) were placed on carbon-coated copper grids for 2 min before removing excess liquid with filter paper, rinsing the grid with deionized water and staining with 2% (w/v) uranyl acetate. TEM images were taken using a FEI Tecnai Spirit G2 BioTWIN TEM.

**Dynamic light scattering (DLS).**—Triplicate DLS measurements were taken at room temperature on a Zetasizer Nano ZSP Zen5600 (Malvern Panalytical) with a scattering angle of 90° and a total measurement time of 3–5 min. The particle size (hydrodynamic radius) and polydispersity index (PDI) were automatically calculated using the manufacturer's software.

**Photothermal measurements.**—Gd-Cy5-TMV-PDA samples (1 mL) were placed in quartz cuvettes and irradiated with an 808-nm near-infrared (NIR) laser (MDL-808-2W) at 1 W cm<sup>-2</sup> for 10 min. Variations in temperature were recorded using an A300 forward-looking infrared (FLIR) thermal camera.

**Photoacoustic measurements.**—Photoacoustic data were collected using a VisualSonics Vevo 2100 LAZR imaging system. Samples were scanned in the wavelength range of 680–970 nm using a 21-MHz centered LZ 250 transducer with a peak energy of  $45 \pm 5$  mJ at 20 Hz at the source. The specimens were aligned at a depth of 1 cm from the transducer and the laser was optimized and calibrated before the measurement.<sup>32</sup>

## Animal experiments

**Ethical statement.**—All animal experiments were carried out in accordance with the guidelines of the Institutional Animal Care and Use Committee (IACUC) of the University of California San Diego (UCSD) and approved by the Animal Ethics committee of UCSD. We used BALB/c 8-week-old female mice (Jackson Laboratory) for all experiments and housed them at the UCSD Moores Cancer Center with unlimited food and water.

**Biodistribution.**—Animals were maintained on an alfalfa-free diet (Teklad 2018S, Harlan Laboratories) for 1 week before random assignment to different cages per time point for each treatment. Animals were retro-orbitally injected with 0.15 mL of 1.333 mg mL<sup>-1</sup> Gd-Cy5-TMV or Gd-Cy5-TMV-PDA particles (200 µg per mouse) or 0.15 mL of PBS as a control. Mice were sacrificed on days 1, 3, 5, 8 and 10, and major organs (kidneys, liver, lungs and spleen) were harvested for three *ex vivo* tests: (1) Sulfo-Cy5 fluorescence measurement using a Xenogen IVIS 200 Optical Imaging System (Caliper Life Sciences): organ samples were imaged side by side with controls to establish the baseline, and the IVIS software was used to determine fluorescence intensity based on region of interest (ROI) analysis. (2) Gd<sup>3+</sup> quantitation by ICP-OES using the equipment described above: weighed pieces of wet organs (500 mg liver, 100 mg lung, 50 mg spleen, and one kidney) were digested in concentrated nitric acid at 100 °C for 15 min and diluted to 5 mL with de-ionized water; Gd ICP Standard (VWR PGD1KN-100) was used to prepare a calibration curve (1–1000 ppb, R<sup>2</sup> = 1.0) for the automated calculation of Gd<sup>3+</sup> concentrations from signal intensities. (3) Detection of PDA: organs were homogenized in 1 mL PBS, and the homogenate was used for photoacoustic measurements as described above.

**Pharmacokinetics (PK).**—Gd-Cy5-TMV or Gd-Cy5-TMV-PDA (200 µg in 150 µL PBS) were administered to mice via tail vein injections. Blood (100 µL) was collected by retro-orbital bleeding after 0, 10, 30, 60, 90, 120, 240, 360, 480 and 1440 min. Blood from time 0 was spiked with 12.7 µg of the VNPs – which is expected in 100 µL blood based on the injected dose (200 µg for the estimated total mouse blood of 1.57 mL). Blood samples were mixed with concentrated nitric acid (200 µL), boiled for 10 min, and diluted to 5 mL with de-ionized water for ICP-OES analysis as described above. Gd<sup>3+</sup> concentrations (ppb) were calculated from a standard calibration curve and the recovered amounts were converted to a percent injected dose (%ID) considering Gd<sup>3+</sup> amounts from time 0 as 100%. The %ID values were plotted against time and fitted to half-life (t<sub>1/2</sub>) calculations using GraphPad Prism v9.0.2.

**Anti-TMV antibody screening and recognition.**—Mice were retro-orbitally injected with 150 µL Gd-Cy5-TMV-PDA (TMV concentration = 1.333 mg mL<sup>-1</sup>; 200 µg per mouse). Four weeks later, blood was collected by retro-orbital bleeding using heparin-coated tubes (Thermo Fisher Scientific). The blood was centrifuged (2000 × g, 4 °C, 10 min) and the plasma was stored at –80 °C for subsequent screening.

**Enzyme-linked immunosorbent assay (ELISA).**—To determine the titers of TMV-specific IgG, 96-well Nunc Polysorb Immuno Plates (Thermo Fisher Scientific) were coated with 10 µg mL<sup>-1</sup> wild-type TMV or Gd-Cy5-TMV-PDA (100 µL per well) in 0.01 M



KP buffer overnight at 4 °C. The coating solution was discarded, and plates were rinsed three times (200 µL per well) with PBS containing 0.05% (v/v) Tween-20 (PBST). The same washing protocol was used between all subsequent steps. We added 3% bovine serum albumin fraction V (Roche) in PBS as a blocking agent (100 µL per well) and plates were incubated for 1 h at room temperature. After blocking, plasma from immunized mice was added at 2x serial dilutions (starting at 1:200 and ending at 1:204,800) in PBS (100 µL per well) and the plates were incubated at room temperature for 1 h. Next, washed plates were incubated at room temperature with horseradish peroxidase (HRP)-conjugated goat anti-mouse IgG Fc secondary antibody (Invitrogen) diluted 1:5000 in PBST for 1 h. After the washing step, plates were developed using 50 µL per well 1-Step Ultra TMB-ELISA substrate (Thermo Fisher Scientific) for 5 min at room temperature, and 50 µL per well of 2 N H<sub>2</sub>SO<sub>4</sub> was added to stop the reaction. Absorbance was measured at 450 nm using a Tecan microplate reader.

**Protein corona preparation and analysis.**—We diluted 50 µL of 0.5 mg mL<sup>-1</sup> Gd-Cy5-TMV or Gd-Cy5-TMV-PDA with 430 µL of PBS and incubated with 10–40 µL human plasma (Sigma-Aldrich) for 1 h at room temperature.<sup>33</sup> Sample aliquots were then analyzed by DLS and TEM as described above, while another aliquot was pelleted by ultracentrifugation (160,000 × g, 4 °C, 45 min), washed three times with PBS and analyzed by SDS-PAGE on 4–12% gels as described above.

**Liquid chromatography mass spectrometry (LC-MS).**—Following SDS-PAGE analysis of the protein corona, the main bands from the Gd-Cy5-TMV-PDA + human plasma gel lane were excised, washed with Millipore water, acetonitrile, 0.1 M ammonium bicarbonate, and acetonitrile again, and then digested with trypsin for LC-MS analysis. Peptides were separated on a nanoLC-Orbitrap XL with the following parameters. A fused silica capillary nanoLC column (pulled to a tip with a Sutter P-2000 laser capillary puller) was packed with Agilent Zorbax C18 particles (5 µm). The capillary inner diameter was 100 µm and the stationary phase was packed with a pressure device to a length of 70 mm. The column was equilibrated with solvent from the Agilent 1100 HPLC pump (solvent A = 0.1% formic acid in water and solvent B = 100% acetonitrile, with several step gradients of 10–90% solvent B). The trypsin-digested sample (3–5 µL redissolved in 15 µL 5% formic acid) was loaded onto the column using a pressure device. The LC gradient program was 1–30% solvent B in 65 min, to 58% solvent B at 77 min, followed by 5 min at 90% solvent B and a return to 1% solvent B at 95 min. The capillary LC was positioned in the nanoelectrospray interface with settings of 1.55 kV source voltage, 40 V capillary voltage, 140 V tube lens, and 165°C capillary temperature. Three microscans were averaged for the ion trap and two for the Fourier transform. There were seven scan events per cycle (6.5 s), one Fourier transform scan (resolution 30,000) from 250–1600 *m/z*, followed by six data-dependent collision induced dissociation (CID) MS/MS scans in the ion trap. Dynamic exclusion was enabled for 40 s with a repeat count of 2. The ion trap CID scans had an isolation width of 2.0 *m/z* and normalized collision energy of 35 eV. After data acquisition, peptide sequence matches (PSM) were found using the OpenMS<sup>34</sup> workflow with the MSGFplus PSM search algorithm.<sup>35</sup> The false discovery rate was set to 5%. Two

variable post-translational modifications per peptide were allowed: oxidation of methionine and deamidation of asparagine.

**Statistical analysis.**—Data were plotted and statistically analyzed using GraphPad Prism 9.0.2. Comparative analysis was carried out with one-way analysis of variance (ANOVA) followed by Tukey's multiple comparison test. Asterisks in the figures indicate significant differences between a study group and the control (\* $p < 0.05$ ; \*\* $p < 0.01$ ; \*\*\* $p < 0.001$ ), whereas hashtags represent significant differences between study groups (# $p < 0.05$ ; ## $p < 0.01$ ; ### $p < 0.001$ ).

## RESULTS AND DISCUSSION

### Particle synthesis and characterization

Wild-type TMV was purified with yields of 11 mg per gram of *N. benthamiana* leaves using an established purification protocol.<sup>30</sup> We converted internal glutamate residues 97 and 106 into alkyne handles with a 100-fold molar excess of propargylamine per coat protein subunit, then simultaneously conjugated them to Gd(DOTA)-azide and sulfo-Cy5-azide using click chemistry (Scheme 1A). Particle concentrations and sulfo-Cy5 loading were characterized by UV-Vis absorption spectrometry (based on the Beer–Lambert law) using extinction coefficient ( $\epsilon_{TMV}$ ) of 3.0 mL mg<sup>-1</sup> cm<sup>-1</sup> at 260 nm for TMV and the molar extinction coefficient ( $\epsilon_{sulfo-Cy5}$ ) of 271,000 L mol<sup>-1</sup> cm<sup>-1</sup> at 647 nm for sulfo-Cy5. Using 0.2 equivalents of sulfo-Cy5-azide per coat protein, data indicated 158 molecules of sulfo-Cy5 per TMV, which is an acceptable loading for bioimaging because fluorescence intensity reaches a plateau at a loading of 222 dye molecules per internally labeled TMV.<sup>36</sup> ICP-OES analysis of samples digested in nitric acid revealed the presence of 1916 chelated Gd<sup>3+</sup> ions per TMV particle, which is much greater than the sulfo-Cy5 loading due to the higher molar excess of Gd(DOTA)-azide (5.2 Gd(DOTA)-azide equivalents per coat protein). The loading of Gd<sup>3+</sup> ions was intentionally higher than that of sulfo-Cy5 to ensure the formulation is suitable for MRI while avoiding concentration-dependent fluorescent quenching during bioimaging.

The particulate nature of the Gd-Cy5-TMV formulation was initially characterized by SEC. We simultaneously detected the viral coat protein at 260 nm, the viral RNA at 280 nm, and sulfo-Cy5 dye at 647 nm. The highest absorbance values at all three wavelengths were observed at an elution volume of 7.8 mL, confirming the co-elution of the three TMV components and thus successful labeling while maintaining structural integrity (Figure 1A). The absence of absorbance at other elution volumes indicates that the particles were intact without significant quantities of broken particles, free proteins, or dye molecules. The 260/280 absorbance ratio for Gd-Cy5-TMV (1.25) was almost the same as wild-type TMV (1.22), which also eluted at 7.8 mL, indicating that labeling does not displace the viral genomic RNA.

Following the protocol previously developed in our lab,<sup>26</sup> Gd-Cy5-TMV particles were coated using 12 mg dopamine per 8 mg particles in alkaline buffer (pH 8.5) for 6 h at room temperature (Scheme 1B,C), purified by centrifugation (25,000 × g, 20 min) and washed with PBS and Millipore water. The resulting Gd-Cy5-TMV-PDA as well as the



Gd-Cy5-TMV particles were then characterized by TEM, which revealed the presence of intact rod-shaped nanoscale particles in both cases (Figure 1B). The surface of the uncoated particles appeared smooth, whereas Gd-Cy5-TMV-PDA featured randomly-distributed knot-like bumps similar to those observed when we coated GdTMV with dopamine under similar conditions. This confirms the tendency for PDA to wrap around the particles and coat them.<sup>26</sup>

SDS-PAGE analysis of the TMV, TMV-PDA, Gd-Cy5-TMV-PDA and Gd-Cy5-TMV samples revealed a band corresponding to the anticipated size of the wild-type TMV coat protein, at ~ 18 kDa (Figure 1C). The Gd- and Cy5-modified coat proteins appear thicker, because it is a mixture of free coat protein and modified coat proteins, where the latter have increased molecular weights and therefore lower mobility. A faint additional 39-kDa band in the TMV-PDA, Gd-Cy5-TMV-PDA and Gd-Cy5-TMV lanes represented coat protein dimers, which are typically observed after bioconjugation reactions.<sup>26,37-39</sup> Imaging the gel under the white or red light before Coomassie staining only revealed the coat protein bands of the dye-labeled particles (Gd-Cy5-TMV-PDA and Gd-Cy5-TMV).

Gd-Cy5-TMV-PDA was characterized in more detail by UV-Vis absorption spectrophotometry, photothermal imaging and photoacoustic analysis. The UV-Vis absorption profile of Gd-Cy5-TMV-PDA was broad (similar to the control PDA) but included spectral features unique to the TMV components (coat protein and RNA at 260–280 nm) as well as the sulfo-Cy5 dye at 647 nm (Figure 2A). Given the photothermal properties of PDA,<sup>40-42</sup> we recorded the temperature profile of Gd-Cy5-TMV-PDA with an infrared camera during irradiation with an 808-nm NIR laser at 1 W/cm<sup>2</sup> (Figure 2B). The particles generated heat in a concentration-dependent manner. The samples heated up continuously for the first 300 s followed by a plateau up to 600 s, which is consistent with previous experiments with 300 s irradiation.<sup>26,27</sup> Photoacoustic behavior was investigated by testing the ability of the particles to emit signals following irradiation at 680–900 nm. Strong signals were observed depending on the wavelength of the pulsed laser: the shortest wavelength (680 nm) yielded the most intense photoacoustic signal for all concentrations tested (Figure 2C). The control (0.1 mg mL<sup>-1</sup> Gd-Cy5-TMV) did not generate a photoacoustic signal. Like the photothermal effects discussed above, the photoacoustic signal intensity was contingent on the concentration of Gd-Cy5-TMV-PDA, as reported for other PDA-coated NPs.<sup>26,43</sup> We observed a linear correlation ( $R^2 = 0.994$ ) between Gd-Cy5-TMV-PDA concentrations (0.005–0.1 mg mL<sup>-1</sup>) and photoacoustic intensities when particles were irradiated at 680 nm (Figures 2D,E). This supports the use of photoacoustic imaging for the detection of PDA in this study.

## Pharmacokinetics

We administered Gd-Cy5-TMV-PDA or Gd-Cy5-TMV by intravenous bolus injection at a dose of 200 µg per mouse to investigate the half-life of the particles in the circulation. Blood samples were taken at regular time points by retro-orbital bleeding and Gd<sup>3+</sup> was quantified by ICP-OES. The %ID in each sample was determined against a calibration curve relative to a time zero blood spiked with the equivalent of a 100% dose, allowing for half-life calculations (Figures 3A and B). The plasma circulation profiles of Gd-Cy5-TMV and Gd-

Cy5-TMV-PDA were distinct: Gd-Cy5-TMV underwent one-phase decay ( $t_{1/2} = 38.77$  min) whereas Gd-Cy5-TMV-PDA underwent two-phase decay (fast  $t_{1/2} = 4.7$  min and slow  $t_{1/2} = 626.2$  min). One-phase decay describes an elimination profile where the body is considered as one blood pool without organs, whereas two-phase decay indicates fast tissue distribution (rapid plasma circulation, short  $t_{1/2}$ ) followed by active tissue clearance or elimination (slower phase with longer  $t_{1/2}$ ).<sup>44</sup> Our PK data thus suggest that PDA coating limits the plasma circulation of Gd-Cy5-TMV, probably reflecting protein corona-induced aggregation that causes rapid organ accumulation (as discussed further below). The PK profile for uncoated particles (Gd-Cy5-TMV) differed from previous experiments in which biphasic decay was observed for Cy5-TMV (fast  $t_{1/2} = 3.5$  min, slow  $t_{1/2} = 94.9$  min) and PEG-Cy5-TMV (fast  $t_{1/2} = 6.3$  min, slow  $t_{1/2} = 44.4$  min).<sup>45</sup> The PK profile also differed from our previous study with Alexa Fluor 647-labeled filamentous potato virus X (PVX) particles, which showed one-phase decay ( $t_{1/2} = 19$  min) whereas PEG-PVX showed two-phase decay (fast  $t_{1/2} = 11$ – $27$  min, slow  $t_{1/2} = 231$ – $1142$  min, depending on the PEG molecular weight).<sup>46</sup> However, the present study cannot be compared directly with these earlier results because we quantified Gd<sup>3+</sup> by ICP-OES rather than fluorescence measurements, which were not reliable in this case due to potential quenching by PDA. The observed fast plasma circulation for Gd-Cy5-TMV-PDA implies the need for surface modifications to facilitate biomedical applications that require longer plasma circulation (e.g., passive tumor targeting through enhanced permeability and retention). Indeed, the PDA surface is easily modified to tailor pharmacological properties,<sup>47,48</sup> and stealth materials such as PEG<sup>45</sup> and serum albumin<sup>31</sup> are suitable because they have already been shown to extend the plasma circulation time of TMV. We therefore investigated the protein corona of Gd-Cy5-TMV-PDA particles in the blood stream, which is responsible for fast plasma clearance.

### Protein corona analysis

NPs in biological fluids adsorb biomolecules to form a surface layer known as the corona. Loosely-bound biomolecules initially form a ‘soft corona’, which is relatively unstable due to the rapid exchange of biomolecules based on their abundance in the medium.<sup>49,50</sup> However, biomolecules with higher affinity for the particle surface ultimately form a ‘hard corona’, which is more stable and defines the particle’s biological identity.<sup>51,52</sup> Depending on the content of the protein corona, the size and surface characteristics of NPs can be slightly or radically modified and can affect their fate *in vivo*, including immune cell uptake, plasma circulation/elimination, tissue distribution and clearance.<sup>53</sup>

In this context, we investigated the protein corona of Gd-Cy5-TMV and Gd-Cy5-TMV-PDA particles by incubating them with human plasma for 1 h. Immediately after incubation, the complexes of particles and plasma proteins were characterized *in situ* by DLS (Figure 4A), zeta potential measurements (Figure 4B) and TEM (Figure 4C). The particles were then pelleted and washed extensively to remove weakly-bound proteins and excess plasma before fractionation of the hard corona by SDS-PAGE and LC-MS (Figure 5).

DLS, zeta potential analysis and TEM revealed variations in particle size distribution, polydispersity index (PDI) and average size. For Gd-Cy5-TMV-PDA, the PDI was 0.48 before incubation and the average size was 302 nm, but these values changed to 0.83 and

1482 nm, respectively after incubation with 10  $\mu$ L of human plasma. For Gd-Cy5-TMV, the PDI was 0.29 before incubation and 0.73 afterwards, but the average size did not change substantially (264 nm before incubation and 279 nm afterwards). Incubation with 20  $\mu$ L of human plasma led to more drastic variations in size distribution patterns, but the changes in PDI and average sizes were inconsistent probably due to the increasing contribution of plasma proteins, which actually compromised the analysis of samples incubated with 40  $\mu$ L human plasma. In all cases, particle size data agreed with the TEM images, which revealed the presence of aggregates only in Gd-Cy5-TMV-PDA + human plasma samples, confirming the general biocompatibility of VNPs as we previously reported.<sup>45,54</sup> Similarly, zeta potential measurements revealed a significant increase in the surface charge of Gd-Cy5-TMV-PDA following incubation with 10  $\mu$ L human plasma (from  $-46$  to  $-15$  mV) whereas there was little change for Gd-Cy5-TMV (from  $-23$  to  $-18$  mV). The zeta potential of human plasma was  $-17$  mV (distribution graph not shown). The varying zeta potential observed for Gd-Cy5-TMV-PDA may not solely reflect corona surface decoration, but also particle agglomeration.<sup>55</sup> Given the initial net charge of Gd-Cy5-TMV-PDA ( $-46$  mV), the induction of aggregation by incubation in plasma suggests some level of heterogeneity on the particle surface, possibly uneven coating with both PDA and the corona, that favors supramolecular interactions over charge-induced repulsion between particles.

Overall, the PDA-coated particles appeared to be much more affected by the protein corona than uncoated particles. This probably reflects the adhesive properties of PDA, owing to its reactivity toward substrates (such as proteins) with amine or thiol groups.<sup>56,57</sup> However, the variation in zeta potential and particle size for Gd-Cy5-TMV-PDA is more likely to be caused by corona-induced aggregation than the thickness of the plasma protein layer on individual particles. Therefore, we envision the use of dispensing excipients (such as PEG) to overcome the corona-induced agglomeration of Gd-Cy5-TMV-PDA.

Particles were incubated with human plasma, washed to remove loosely-bound proteins, and analyzed with SDS-PAGE. The SDS-PAGE gels revealed multiple hard corona protein bands adsorbed to the coated and uncoated particles (Figure 5A). Remarkably, we observed a  $\sim 198$ -kDa band solely in the lane representing the coated particles (Figure 5A,B). Quantitative analysis by densitometry revealed that the hard corona proteins surrounding the Gd-Cy5-TMV-PDA particles were 2–10-fold more abundant than those on the uncoated (Gd-Cy5-TMV) particles (Table 1). We previously detected fewer plasma proteins in the TMV corona compared to synthetic SiO<sub>2</sub> particles.<sup>54</sup> This can be explained by the heterogeneous zwitterionic surface of proteinaceous VNPs, which leads to fewer interactions with other zwitterionic biomolecules such as plasma proteins.<sup>58,59</sup>

LC-MS analysis of protein bands in the Gd-Cy5-TMV-PDA hard corona revealed the presence of more than 100 plasma proteins (the 21 most abundant are listed in Table 2). The most abundant were immunoglobulins (55.6%), followed by complement factors (14%), albumins (13%) and fibrinogens (2%). All of these proteins have been identified before in the protein corona of synthetic NPs based on silica<sup>60</sup> and iron oxide<sup>61</sup>, but also in VNPs such as TMV<sup>54</sup> and physalis mottle virus (PhMV).<sup>62</sup> Immunoglobulins and complement factors are opsonins, which tag NPs in plasma and facilitate their uptake by immune cells (thus removing them from the bloodstream), as well as subsequent entrapment in the

organs of the reticuloendothelial system (RES), such as the spleen, liver and lungs.<sup>63,64</sup> In contrast, albumins and coagulation proteins such as fibrinogens are classed as dysopsonins because they confer stealth properties by preventing phagocytosis, thus extending the plasma circulation time.<sup>60,62</sup> Gd-Cy5-TMV-PDA is predominantly covered by opsonins, with dysopsonins representing a much smaller fraction, which may explain the decreased plasma retention of Gd-Cy5-TMV-PDA.

The 198-kDa band found only on the Gd-Cy5-TMV-PDA particles contained immunoglobulin kappa light chains (66.8%), the TMV coat protein (32.47%), and the tyrosine protein kinase ABL1 (0.73%) (Table 2). The tyrosine protein kinase is the only protein that has not yet been reported in the corona of NPs. However, considering its low abundance in the Gd-Cy5-TMV-PDA corona (< 0.3%) and physiological activity (as a cytoplasmic tyrosine kinase regulating cell growth and differentiation),<sup>65</sup> this protein is unlikely to affect the systemic trafficking of Gd-Cy5-TMV-PDA. It is also important to note that the identified immunoglobulin kappa chains represented only 31.6% of all immunoglobulins identified in the corona of Gd-Cy5-TMV-PDA. Gamma immunoglobulins were the most abundant (64.5%) and lambda immunoglobulins were the least abundant (3.6%). However, the affinity of kappa light chains for Gd-Cy5-TMV-PDA could be tailored to target immune cells for epitope display or to target lymphoma and chronic lymphocytic leukemia cells expressing monoclonal immunoglobulins with kappa light chains.<sup>66</sup>

Immunoglobulins are expected to be part of the VNP corona because plant viruses are known to be immunogenic.<sup>46</sup> On this basis, one would predict that the corona of uncoated Gd-Cy5-TMV contains more immunoglobulins than PDA-coated particles, but the opposite was revealed in our experiments, suggesting that the surface of Gd-Cy5-TMV-PDA still displayed some proteinaceous features. This is supported by the fact that anti-TMV antibodies can recognize and bind to Gd-Cy5-TMV-PDA although this is to a lesser extent compared to uncoated Gd-Cy5-TMV (discussed below). Another important observation was the presence of TMV coat proteins in the corona (~65 to ~198 kDa), confirming this was indeed the hard corona strongly bound to the TMV surface, possibly via the reactive PDA catechol backbone.<sup>57,67</sup> The easy decoration of the PDA coat with corona proteins confirms the potential for PDA-primer coating to facilitate particle loading with various cargo molecules including drugs,<sup>68</sup> targeting ligands,<sup>69</sup> and antibodies.<sup>48</sup> Gd-Cy5-TMV-PDA complexes with plasma proteins could be tailored further to minimize particle aggregation and support important biomedical applications such as targeted delivery to RES organs. Even so, the Gd-Cy5-TMV-PDA protein corona may be responsible for the quicker plasma clearance compared to uncoated Gd-Cy5-TMV particles, indicating that further surface modification is required for extended plasma circulation. We are optimistic that this can be achieved because PDA surface modification has been reported in previous studies for several biomedical applications.<sup>47,48,67-69</sup>

### Production and recognition of anti-TMV antibodies

Having detected immunoglobulins in the Gd-Cy5-TMV-PDA protein corona, we investigated the immune response to determine whether Gd-Cy5-TMV-PDA can elicit and be recognized by TMV-specific antibodies. Gd-Cy5-TMV-PDA (200 µg) was administered

to mice by retro-orbital injection, and blood samples were collected immediately (week 0) and on week 4. Plasma was assessed for TMV-specific antibodies by ELISA using plates coated with Gd-Cy5-TMV-PDA or wild-type TMV (Figure 6A). Regardless of the plate coating, TMV-specific antibodies were significantly more abundant at week 4 compared to week 0 (Figure 6B). This indicates the production of TMV-specific antibodies following the administration of Gd-Cy5-TMV-PDA and confirms the uptake and intracellular processing of Gd-Cy5-TMV-PDA by immune cells,<sup>70</sup> in agreement with the presence of opsonins among the identified corona proteins (Table 2). Although we observed a reactive antibody response, the TMV-specific immunoglobulins recognized wild-type TMV much more efficiently than Gd-Cy5-TMV-PDA (Figure 6C). This is consistent with our previous analysis of PEG-TMV and TMV coated with serum albumin (SA-TMV), both of which elicited an antibody response but with lower recognition compared to wild-type TMV.<sup>31,70</sup> TMV is widespread in nature (*e.g.*, the food chain, agriculture and tobacco products), so pre-existing immunity against TMV is common, with TMV-specific antibodies detected in plasma from healthy smokers, smokeless-tobacco users, and non-smokers.<sup>71</sup> Accordingly, the ability of PDA to suppress recognition by TMV-specific antibodies is an asset for the clinical application of Gd-Cy5-TMV-PDA particles, given the prevalence of such antibodies in humans and their production following the repeated administration of VNPs.<sup>70</sup>

### Biodistribution and tissue clearance

The distribution of PDA-coated and uncoated Gd-Cy5-TMV particles to organs was assessed following the retro-orbital injection of mice with a dose of 200  $\mu$ g. Animals were euthanized at different time points (days 1, 3, 5, 8 and 10) and major organs (kidneys, liver, lungs and spleen) were harvested for particle localization *ex vivo*. Organs were analyzed with IVIS imaging for Cy5, ICP-OES for Gd<sup>3+</sup> following digestion in nitric acid, and the photoacoustic detection of PDA in homogenates. Fluorescence imaging indicated that Gd-Cy5-TMV was present in the liver, lungs and spleen for up to 3 days, and Gd-Cy5-TMV-PDA was present solely in the lungs for up to 5 days (Figure S1). However, quantitative fluorescence analysis using ROI measurements showed that Gd-Cy5-TMV was present in the liver for up to 5 days and in the spleen for as long as 8 days (Figure 7A), whereas Gd-Cy5-TMV-PDA was present only in the lungs for up to 5 days, in agreement with the imaging data. The distribution of Gd-Cy5-TMV based on fluorescence data agreed with the biodistribution previously reported for Cy5-TMV, where particles were found mainly in the liver and the spleen for up to 4 days.<sup>45</sup>

The fluorescence signal for Gd-Cy5-TMV-PDA (in the lungs) was much weaker compared to Gd-Cy5-TMV (in all organs), indicating fluorescence quenching by PDA<sup>72</sup>. Given this limitation, the quantitative analysis of Gd<sup>3+</sup> was considered more reliable for the assessment of biodistribution. Unlike fluorescence detection, Gd<sup>3+</sup> from Gd-Cy5-TMV-PDA was detected in the liver, lungs and spleen for more than 10 days (Figure 7B). The Gd-based biodistribution of Gd-Cy5-TMV was consistent with the fluorescence data: high concentrations of Gd<sup>3+</sup> were detected in the liver and spleen, but Gd<sup>3+</sup> from Gd-Cy5-TMV persisted much longer in these organs (10 days) than suggested by the fluorescence data (5 days) and, for unknown reasons, there was no Gd<sup>3+</sup> signal in the lungs (whereas fluorescence from Gd-Cy5-TMV was apparent on day 1).



Based on the localization of Cy5 and  $Gd^{3+}$ , it is evident that the distribution of PDA-coated and uncoated particles differs mainly in terms of the lungs. This stands to reason because the Gd-Cy5-TMV-PDA particles featured a more extensive protein corona, which promotes aggregation and can explain accumulation in the lungs.<sup>73</sup> We previously observed the presence of other surface-modified TMV particles in the lungs: Dy-TMV decorated with integrin  $\alpha\beta_1$  ligands and PEGylated Dy-TMV were both found to accumulate mainly in the liver, lungs and spleen, but good tumor homing was still observed.<sup>23</sup> The accumulation of NPs in RES organs is often attributed to the ability of cells of the mononuclear phagocytic system (e.g., macrophages) to take up such particles,<sup>63,64</sup> which is facilitated by the presence of opsonins among the corona proteins, as observed for Gd-Cy5-TMV-PDA. However, in addition to the potential impact of immune cell uptake on the distribution of Gd-Cy5-TMV-PDA, increase in nanoparticle size due to protein corona formation and corona-induced aggregation (as shown in Figure 4) need to be considered among the driving forces for pulmonary distribution and clearance of Gd-Cy5-TMV-PDA. Lung accumulation of nanoparticle aggregates has been reported with other virus-based and synthetic NPs.<sup>23,73</sup>

Although the detection of Cy5 and  $Gd^{3+}$  revealed similar organ distributions, the clearance profiles were faster for Cy5 (5 days) than  $Gd^{3+}$  (10 days). This discrepancy makes the assessment of tissue clearance more complex, given that previous studies reported faster tissue clearance for TMV-based particles (4 days).<sup>45</sup> The detection of  $Gd^{3+}$  at later time points may reflect particle degradation, and should not be considered as evidence of long-lasting particle residence within organs. To evaluate particle intactness and clearance, we investigated the photoacoustic activity of homogenized lungs and liver as major organs to track the fate of PDA (Figures 7C,D). We detected strong photoacoustic signals in both organs up to day 8. Because PDA is biodegradable, no photoacoustic signal should be detected when the coat is removed, so it is possible that the observed photoacoustic signals may indicate that Gd-Cy5-TMV-PDA particles are present and intact. The co-localization of  $Gd^{3+}$  and PDA in the liver and lungs for up to 8 days suggests that Gd-Cy5-TMV-PDA particles remained stable over this time period.

The comparison of coated and uncoated particles revealed that Gd-Cy5-TMV-PDA particles can be distinguished by their specific accumulation in the lung and their 8-day tissue residence time, whereas Gd-Cy5-TMV only accumulated in the liver and spleen and the residence time was 5 days for both the Cy5 and  $Gd^{3+}$  tags. The PDA coat therefore extends the tissue residence of TMV particles. To some degree, this prolonged tissue residence may be attributed to the fact that the PDA-coated TMV particles aggregated due to more intensive protein corona formation. In the form of aggregates, the surface-to-volume ratio of VNPs is reduced and slower break-down of these larger aggregates may be the underlying reason for this observation. The Gd-Cy5-TMV-PDA particles degraded over time, and by day 10 the three tags no longer co-localized in the lungs and liver, suggesting particle disintegration into separate components (Figure 8). Indeed, 8 days appears to be an ideal tissue clearance time given the biocompatibility of VNPs,<sup>17</sup> especially when compared to inorganic particles<sup>74</sup> and carbon nanotubes<sup>75</sup> that can persist in tissues for more than a month. The PDA coating can also prolong the tissue residence of gold NPs, which remained stable in mouse liver and spleen for 42 days without overt toxicity.<sup>76</sup> It is possible that the intrinsic biodegradability of TMV facilitated the degradation of Gd-Cy5-TMV-PDA



particles within 8 days. The slow tissue degradation of PDA systems has been exploited in biomedical applications such as tissue engineering.<sup>77</sup> Accordingly, we propose that the longer tissue residence of PDA-coated vs uncoated Gd-Cy5-TMV particles would be beneficial for theranostic applications by adding the potential for sustained local drug delivery to the multimodal MRI, photoacoustic imaging and photothermal capabilities.

## CONCLUSION

To investigate the *in vivo* fate of PDA-coated Gd-Cy5-TMV particles, TMV particles were internally co-labeled with Gd<sup>3+</sup> complexes and the fluorescent dye Cy5. The Gd-Cy5-TMV particles were coated with the biopolymer PDA to yield Gd-Cy5-TMV-PDA particles, and both coated and uncoated particles were characterized *in vivo* by profiling their plasma circulation/PK, protein corona, immunoglobulin attachment, organ distribution and clearance. We found that Gd-Cy5-TMV-PDA particles have a shorter plasma circulation and broader biodistribution than uncoated Gd-Cy5-TMV particles. The uncoated particles were mainly distributed to the liver and spleen, whereas the Gd-Cy5-TMV-PDA particles were detected in the liver, lungs and spleen, one of the typical biodistribution profiles promoted by corona-induced aggregation.<sup>23</sup> We predict that the surface modification of Gd-Cy5-TMV-PDA with stealth biomaterials (such as serum albumin or PEG)<sup>47</sup> would tune the interactions with plasma proteins and enhance *in vivo* performance for systemic applications. We found that Gd-Cy5-TMV-PDA persists for longer than uncoated particles in tissues (8 vs 5 days) but is cleared at a typical rate for biodegradable protein-based NPs and much more rapidly than PDA-coated synthetic counterparts such as gold NPs.<sup>76</sup> The administration of Gd-Cy5-TMV-PDA elicited anti-TMV antibodies, confirming the particles are processed by immune cells, but the antibodies bind less efficiently to Gd-Cy5-TMV-PDA than wild-type TMV. Given the prevalence of anti-TMV antibodies in the human population, the ability of Gd-Cy5-TMV-PDA to evade immunosurveillance is an asset for effective systemic and repeated administrations. The multifunctional features of Gd-Cy5-TMV-PDA (including its high aspect ratio and suitability for MRI, photoacoustic imaging, and photothermal activity) set the stage for the future engineering and efficacy testing of PDA-coated proteinaceous NPs.

## Supplementary Material

Refer to Web version on PubMed Central for supplementary material.

## Acknowledgements

The authors acknowledge the UCSD Molecular Mass Spectrometry Facility for the LC/MS analysis of corona proteins.

## Funding

This work was supported in part via the NIH grant R01 CA202814. JVJ acknowledges NIH support under DP2 HL137187 and S10 OD021821.

## REFERENCES

1. Gallo E, Diaferia C, Di Gregorio E, Morelli G, Gianolio E, Accardo A Peptide-Based Soft Hydrogels Modified with Gadolinium Complexes as MRI Contrast Agents. *Pharmaceuticals*. 2020, 13(2), 19. 10.3390/ph13020019.
2. Böll K, Zimpel A, Dietrich O, Wuttke S & Peller M Clinically Approved MRI Contrast Agents as Imaging Labels for a Porous Iron-Based MOF Nanocarrier: A Systematic Investigation in a Clinical MRI Setting. *Adv. Ther* 2020, 3, 1900126.
3. Wang Z, Carniato F, Xie Y, Huang Y, Li Y, He S, Zang N, Rinehart JD, Botta M, Gianneschi NC High Relaxivity Gadolinium-Polydopamine Nanoparticles. *Small*. 2017, 13(43). doi: 10.1002/sml.201701830.
4. Caravan P, Farrar CT, Frullano L & Uppal R Influence of molecular parameters and increasing magnetic field strength on relaxivity of gadolinium- and manganese-based T1 contrast agents. *Contrast Media Mol. Imaging* 2009, 4, 89–100. [PubMed: 19177472]
5. Chen R, Ling D, Zhao L, Wang S, Liu Y, Bai R, Baik S, Zhao Y, Chen C, Hyeon T Parallel Comparative Studies on Mouse Toxicity of Oxide Nanoparticle- and Gadolinium-Based T1 MRI Contrast Agents. *ACS Nano* 2015, 9, 12425–12435. [PubMed: 26567968]
6. Penfield JG & Reilly RF What nephrologists need to know about gadolinium. *Nat. Clin. Pract. Nephrol* 2007, 3, 654–668. [PubMed: 18033225]
7. Botta M & Tei L Relaxivity enhancement in macromolecular and nanosized Gd III-based MRI contrast agents. *Eur. J. Inorg. Chem* 2012, 12, 1945–1960.
8. Bulte JWM & Daldrop-Link HE Clinical tracking of cell transfer and cell transplantation: Tu. *Radiology* 2018, 289, 604–615. [PubMed: 30299232]
9. Caravan P Strategies for increasing the sensitivity of gadolinium based MRI contrast agents. *Chem. Soc. Rev* 2006, 35, 512–523. [PubMed: 16729145]
10. Rudramurthy GR & Swamy MK Potential applications of engineered nanoparticles in medicine and biology: an update. *J. Biol. Inorg. Chem* 2018. doi:10.1007/s00775-018-1600-6.
11. Wallyn J, Anton N, Akram S & Vandamme TF Biomedical Imaging : Principles , Technologies, Clinical Aspects, Contrast Agents, Limitations and Future Trends in Nanomedicines. *Pharm Res* 2019, 36(6), 78. doi: 10.1007/s11095-019-2608-5.. [PubMed: 30945009]
12. Aaron AJ, Bumb A & Brechbiel MW Macromolecules, dendrimers, and nanomaterials in magnetic resonance imaging: The interplay between size, function, and pharmacokinetics. *Chem. Rev* 2010, 110, 2921–2959. [PubMed: 20067234]
13. Johnson NJJ, He S, Nguyen Huu VA & Almutairi A Compact Micellization: A Strategy for Ultrahigh T1 Magnetic Resonance Contrast with Gadolinium-Based Nanocrystals. *ACS Nano* 2016, 10, 8299–8307. [PubMed: 27588579]
14. Anselmo AC & Mitragotri S Nanoparticles in the clinic: An update. *Bioeng. Transl. Med* 2019, 4(3), e10143. doi: 10.1002/btm2.10143 [PubMed: 31572799]
15. Crist RM, Dasa SS, Liu CH, Clogston JD, Dobrovolskaia MA, Stern ST Challenges in the development of nanoparticle-based imaging agents: Characterization and biology. *Wiley Interdiscip. Rev. Nanomedicine Nanobiotechnology* 2020, 13, e1665. DOI: 10.1002/wnan.1665 [PubMed: 32830448]
16. Jeevanandam J, Pal K & Danquah MK Virus-like nanoparticles as a novel delivery tool in gene therapy. *Biochimie* 2019, 157, 38–47. [PubMed: 30408502]
17. Nkanga CI & Steinmetz NF The pharmacology of plant virus nanoparticles. *Virology* 2021, 556, 39–61. [PubMed: 33545555]
18. Alemzadeh E, Dehshahri A, Izadpanah K & Ahmadi F Plant virus nanoparticles: Novel and robust nanocarriers for drug delivery and imaging. *Colloids Surfaces B Biointerfaces* 2018, 167, 20–27. [PubMed: 29625419]
19. Chung YH, Cai H & Steinmetz NF Viral nanoparticles for drug delivery, imaging, immunotherapy, and theranostic applications. *Adv. Drug Deliv. Rev* 2020, 156, 214–235. [PubMed: 32603813]
20. Prasuhn DE, Yeh RM, Obenaus A & Finn MG Viral MRI contrast agents : coordination of Gd by native virions and attachment of Gd complexes by azide – alkyne cycloaddition. *Chem. Commun* 2007, 12, 1269–1271. doi:10.1039/b615084e.

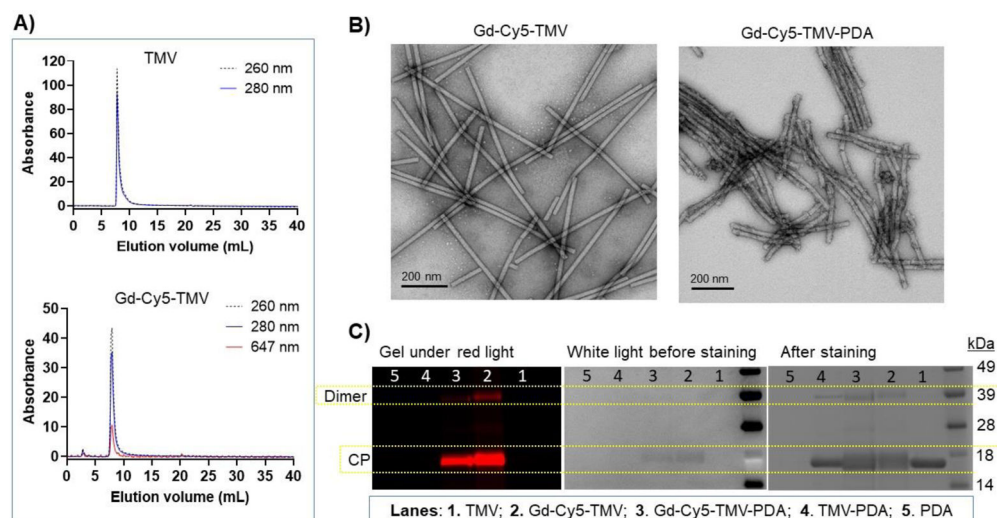
21. Anderson EA, Isaacman S, Peabody DS, Wang EY, Canary JW, & Kirshenbaum K Viral nanoparticles donning a paramagnetic coat: Conjugation of MRI contrast agents to the MS2 capsid. *Nano Lett.* 2006, 6, 1160–1164. [PubMed: 16771573]
22. Allen M, Bulte JW, Liepold L, Basu G, Zywicke HA, Frank JA, Young M & Douglas T Paramagnetic viral nanoparticles as potential high-relaxivity magnetic resonance contrast agents. *Magn. Reson. Med* 2005, 54, 807–812. [PubMed: 16155869]
23. Hu H, Zhang Y, Shukla S, Gu Y, Yu X, & Steinmetz NF Dysprosium-Modified Tobacco Mosaic Virus Nanoparticles for Ultra-High-Field Magnetic Resonance and Near-Infrared Fluorescence Imaging of Prostate Cancer. *ACS Nano* 2017, 11, 9249–9258. [PubMed: 28858475]
24. Bruckman MA, Hern S, Jiang K, Flask CA, Yu X, & Steinmetz NF Tobacco mosaic virus rods and spheres as supramolecular high-relaxivity MRI contrast agents. *J. Mater. Chem. B* 2013, 1, 1482–1490. [PubMed: 23589767]
25. Bruckman MA, Jiang K, Simpson EJ, Randolph LN, Luyt LG, Yu X, & Steinmetz NF Dual-modal magnetic resonance and fluorescence imaging of atherosclerotic plaques in vivo using VCAM-1 targeted tobacco mosaic virus. *Nano Lett.* 2014, 14, 1551–1558. [PubMed: 24499194]
26. Hu H, Yang Q, Baroni S, Yang H, Aime S, & Steinmetz NF Polydopamine-decorated tobacco mosaic virus for photoacoustic/magnetic resonance bimodal imaging and photothermal cancer therapy. *Nanoscale* 2019, 11, 9760–9768. [PubMed: 31066418]
27. Seth A, Gholami Derami H, Gupta P, Wang Z, Rathi P, Gupta R, Cao T, Morrissey JJ & Singamaneni S Polydopamine-Mesoporous Silica Core-Shell Nanoparticles for Combined Photothermal Immunotherapy. *ACS Appl. Mater. Interfaces* 2020, 12(38), 42499–42510. [PubMed: 32838525]
28. Nam J, Son S, Ochyl LJ, Kuai R, Schwendeman A, & Moon JJ Chemo-photothermal therapy combination elicits anti-tumor immunity against advanced metastatic cancer. *Nat. Commun* 2018, 9, 1074 10.1038/s41467-018-03473-9 [PubMed: 29540781]
29. Lemaster JE, Wang Z, Hariri A, Chen F, Hu Z, Huang Y, Barback CV, Cochran R, Gianneschi NC & Jokerst JV Gadolinium Doping Enhances the Photoacoustic Signal of Synthetic Melanin Nanoparticles: A Dual Modality Contrast Agent for Stem Cell Imaging. *Chem. Mater* 2019, 31, 251–259. [PubMed: 33859455]
30. Bruckman MA & Steinmetz NF Chemical Modification of the Inner and Outer Surfaces of Tobacco Mosaic Virus (TMV). *Virus Hybrids as Nanomater. Methods Protoc.* ed. B. Lin B. Ratna 2020, 1108, 173–185.
31. Pitek AS, Jameson SA, Veliz FA, Shukla S & Steinmetz NF Serum albumin ‘camouflage’ of plant virus based nanoparticles prevents their antibody recognition and enhances pharmacokinetics. *Biomaterials* 2016, 89, 89–97. [PubMed: 26950168]
32. Zhou J & Jokerst JV Photoacoustic imaging with fiber optic technology: A review. *Photoacoustics* 2020, 20, 100211. 10.1016/j.pacs.2020.100211 [PubMed: 33163358]
33. Caracciolo G, Caputo D, Pozzi D, Colapicchioni V & Coppola R Size and charge of nanoparticles following incubation with human plasma of healthy and pancreatic cancer patients. *Colloids Surfaces B Biointerfaces* 2014, 123, 673–678. [PubMed: 25456990]
34. Röst HL, Sachsenberg T, Aiche S, Bielow C, Weisser H, Aicheler F, et al. OpenMS: A flexible open-source software platform for mass spectrometry data analysis. *Nat. Methods* 2016, 13, 741–748. [PubMed: 27575624]
35. Kim S & Pevzner PA MS-GF+ makes progress towards a universal database search tool for proteomics. *Nat. Commun* 2014, 5, 5277. 10.1038/ncomms6277 [PubMed: 25358478]
36. Wen AM, Infusino M, De Luca A, Kernan DL, Czapar AE, Strangi G, & Steinmetz NF Interface of Physics and Biology: Engineering Virus-Based Nanoparticles for Biophotonics. *Bioconjugate Chem.* 2015, 26, 51–62.
37. Gulati NM, Pitek AS, Steinmetz NF & Stewart PL Cryo-electron tomography investigation of serum albumin-camouflaged tobacco mosaic virus nanoparticles. *Nanoscale* 2017, 9, 3408–3415. [PubMed: 28112764]
38. Park J, Gao H, Wang Y, Hu H, Simon DI, & Steinmetz NF S100A9-targeted tobacco mosaic virus nanoparticles exhibit high specificity toward atherosclerotic lesions in ApoE<sup>-/-</sup> mice. *J. Mater. Chem. B* 2019, 7(11), 1842–1846. [PubMed: 32255046]

39. Wen AM, Infusino M, De Luca A, Kernan DL, Czapar AE, Strangi G, & Steinmetz NF Interface of physics and biology: Engineering virus-based nanoparticles for biophotonics. *Bioconjug. Chem* 2015, 26, 51–62. [PubMed: 25541212]
40. Chen R, Zhu C, Fan Y, Feng W, Wang J, Shang E, Zhou Q, & Chen Z Polydopamine-Based Multifunctional Platform for Combined Photothermal Therapy, Chemotherapy, and Immunotherapy in Malignant Tumor Treatment. *ACS Appl. Bio Mater* 2019, 2, 874–883.
41. Poinard B, Neo SZY, Yeo ELL, Heng HPS, Neoh KG, & Kah JCY Polydopamine Nanoparticles Enhance Drug Release for Combined Photodynamic and Photothermal Therapy. *ACS Appl. Mater. Interfaces* 2018, 10, 21125–21136. [PubMed: 29871485]
42. Zhang P, Xu Q, Li X & Wang Y pH-responsive polydopamine nanoparticles for photothermally promoted gene delivery. *Mater. Sci. Eng. C* 2020, 108, 110396.
43. Yim W, Zhou J, Mantri Y, Creyer MN, Moore CA, & Jokerst JV Gold Nanorod-Melanin Hybrids for Enhanced and Prolonged Photoacoustic Imaging in the Near-Infrared-II Window. *ACS Appl. Mater. Interfaces* 2021, 13, 14974–14984. [PubMed: 33761255]
44. Raza K, Kumar P, Kumar N & Malik R Pharmacokinetics and biodistribution of the nanoparticles. *In Advances in nanomedicine for the delivery of therapeutic nucleic acids*. Woodhead publishing 2017, 166–186. doi:10.1016/B978-0-08-100557-6.00009-2.
45. Bruckman MA, Randolph LN, VanMeter A, Hern S, Shoffstall AJ, Taurog RE, & Steinmetz NF Biodistribution, pharmacokinetics, and blood compatibility of native and PEGylated tobacco mosaic virus nano-rods and -spheres in mice. *Virology* 2014, 449, 163–173. [PubMed: 24418549]
46. Lee KL, Shukla S, Wu M, Ayat NR, El Sanadi CE, Wen AM, Edelbrock JF, Pokorski JK, Commandeur U, Dubyak GR & Steinmetz NF Stealth filaments: Polymer chain length and conformation affect the in vivo fate of PEGylated potato virus X. *Acta Biomater.* 2015, 19, 166–179. [PubMed: 25769228]
47. Liu J, Xu H, Tang X, Xu J, Jin Z, Li H, Wang S, Gou J & Jin X Simple and tunable surface coatings via polydopamine for modulating pharmacokinetics, cell uptake and biodistribution of polymeric nanoparticles. *RSC Adv.* 2017, 7(26), 15864–15876.
48. Black KCL, Yi J, Rivera JG, Zelasko-Leon DC & Messersmith PB Polydopamine-enabled surface functionalization of gold nanorods for cancer cell-targeted imaging and photothermal therapy. *Nanomedicine* 2013, 8, 17–28. [PubMed: 22891865]
49. Rampado R, Crotti S, Caliceti P, Pucciarelli S & Agostini M Recent Advances in Understanding the Protein Corona of Nanoparticles and in the Formulation of “Stealthy” Nanomaterials. *Front. Bioeng. Biotechnol* 2020, 8, 1–19. [PubMed: 32039188]
50. Mohammad-Beigi H, Hayashi Y, Zeuthen CM, Eskandari H, Scavenius C, Juul-Madsen K, Vorup-Jensen T, Enghild JJ & Sutherland DS Mapping and identification of soft corona proteins at nanoparticles and their impact on cellular association. *Nat. Commun* 2020, 11, 4535. 10.1038/s41467-020-18237-7 [PubMed: 32913217]
51. Milani S, Baldelli Bombelli F, Pitek AS, Dawson KA & Rädler J Reversible versus irreversible binding of transferrin to polystyrene nanoparticles: Soft and hard corona. *ACS Nano* 2012, 6, 2532–2541. [PubMed: 22356488]
52. Yu Q, Zhao L, Guo C, Yan B & Su G Regulating Protein Corona Formation and Dynamic Protein Exchange by Controlling Nanoparticle Hydrophobicity. *Front. Bioeng. Biotechnol* 2020, 8, 210. doi: 10.3389/fbioe.2020.00210. [PubMed: 32266237]
53. Monopoli MP, Walczyk D, Campbell A, Elia G, Lynch I, Baldelli Bombelli F, & Dawson KA Physical-Chemical aspects of protein corona: Relevance to in vitro and in vivo biological impacts of nanoparticles. *J. Am. Chem. Soc* 2011, 133, 2525–2534. [PubMed: 21288025]
54. Pitek AS, Wen AM, Shukla S & Steinmetz NF The Protein Corona of Plant Virus Nanoparticles Influences their Dispersion Properties, Cellular Interactions, and in Vivo Fates. *Small* 2016, 12, 1758–1769. [PubMed: 26853911]
55. Nkanga CI & Krause RWM Encapsulation of Isoniazid-conjugated Phthalocyanine-In-Cyclodextrin-In-Liposomes Using Heating Method. *Sci. Rep* 2019, 9, 11485. [PubMed: 31391517]

56. Liu Y, Ai K & Lu L Polydopamine and its derivative materials: Synthesis and promising applications in energy, environmental, and biomedical fields. *Chem. Rev* 2014, 114, 5057–5115. [PubMed: 24517847]
57. Ryu JH, Messersmith PB & Lee H Polydopamine Surface Chemistry: A Decade of Discovery. *ACS Appl. Mater. Interfaces* 2018, 10, 7523–7540. [PubMed: 29465221]
58. Berardi A, Baldelli Bombelli F, Thuenemann EC & Lomonosoff GP Viral nanoparticles can elude protein barriers: Exploiting rather than imitating nature. *Nanoscale* 2019, 11, 2306–2316. [PubMed: 30662985]
59. Abdulkarim M, Agulló N, Cattoz B, Griffiths P, Bernkop-Schnürch A, Borros SG, & Gumbleton M Nanoparticle diffusion within intestinal mucus: Three-dimensional response analysis dissecting the impact of particle surface charge, size and heterogeneity across polyelectrolyte, pegylated and viral particles. *Eur. J. Pharm. Biopharm* 2015, 97, 230–238. [PubMed: 25661585]
60. Tenzer S, Docter D, Rosfa S, Wlodarski A, Kuharev J, Rekik A, et al. Nanoparticle size is a critical physicochemical determinant of the human blood plasma corona: A comprehensive quantitative proteomic analysis. *ACS Nano* 2011, 5, 7155–7167. [PubMed: 21866933]
61. Chen F, Wang G, Griffin JI, Brenneman B, Banda NK, Holers VM, Backos DS, Wu L, Moghimi SM & Simberg D Complement proteins bind to nanoparticle protein corona and undergo dynamic exchange in vivo. *Nat. Nanotechnol* 2017, 12, 387–393. [PubMed: 27992410]
62. Hu H, Masarapu H, Gu Y, Zhang Y, Yu X, & Steinmetz NF Physalis Mottle Virus-like Nanoparticles for Targeted Cancer Imaging. *ACS Appl. Mater. Interfaces* 2019, 11, 18213–18223. [PubMed: 31074602]
63. Dobrovolskaia MA, Germolec DR & Weaver JL Evaluation of nanoparticle immunotoxicity. *Nat. Nanotechnol* 2009, 4, 411–414. [PubMed: 19581891]
64. Dobrovolskaia MA & McNeil SE Immunological properties of engineered nanomaterials. *Nanosci. Technol. A Collect. Rev. from Nat. Journals* 2009, 278–287. doi:10.1142/9789814287005\_0029.
65. Diculescu VC & Enache TA Electrochemical evaluation of Abelson tyrosine-protein kinase 1 activity and inhibition by imatinib mesylate and danusertib. *Anal. Chim. Acta* 2014, 845, 23–29. [PubMed: 25201268]
66. Vera J, Savoldo B, Vigouroux S, Biagi E, Pule M, Rossig C, Wu J, Heslop HE, Rooney CM, Brenner MK & Dotti G T lymphocytes redirected against the  $\kappa$  light chain of human immunoglobulin efficiently kill mature B lymphocyte-derived malignant cells. *Blood* 2006, 108, 3890–3897. [PubMed: 16926291]
67. Lee H, Rho J & Messersmith PB Facile conjugation of biomolecules onto surfaces via mussel adhesive protein inspired coatings. *Adv. Mater* 2009, 21, 431–434. [PubMed: 19802352]
68. Cui J, Yan Y, Such GK, Liang K, Ochs CJ, Postma A, & Caruso F Immobilization and intracellular delivery of an anticancer drug using mussel-inspired polydopamine capsules. *Biomacromolecules* 2012, 13, 2225–2228. [PubMed: 22792863]
69. Zhao L, Bi D, Qi X, Guo Y, Yue F, Wang X, & Han M Polydopamine-based surface modification of paclitaxel nanoparticles for osteosarcoma targeted therapy. *Nanotechnology* 2019, 30(25), 255101. [PubMed: 30736019]
70. Gulati NM, Pitek AS, Czapar AE, Stewart PL & Steinmetz NF The in vivo fates of plant viral nanoparticles camouflaged using self-proteins: Overcoming immune recognition. *J. Mater. Chem. B* 2018, 6, 2204–2216. [PubMed: 30294445]
71. Liu R, Vaishnav RA, Roberts AM & Friedland RP Humans Have Antibodies against a Plant Virus : Evidence from Tobacco Mosaic Virus. *PLoS One* 2013, 8, e60621. [PubMed: 23573274]
72. Mao W, Hu C, Zheng H, Xie J, Shi X, Du Y, & Wang F A Functionalized Polydopamine Theranostic Nanoprobe for Efficient Imaging of miRNA-21 and In Vivo Synergetic Cancer Therapy. *Mol. Ther. - Nucleic Acids* 2020, 22, 27–37. [PubMed: 32911342]
73. An L, Hu H, Du J, Wei J, Wang L, Yang H, Wu D, Shi H, Li F & Yang S Paramagnetic hollow silica nanospheres for in vivo targeted ultrasound and magnetic resonance imaging. *Biomaterials* 2014, 35, 5381–5392. [PubMed: 24703718]
74. Gad SC, Sharp KL, Montgomery C, Payne JD & Goodrich GP Evaluation of the toxicity of intravenous delivery of auroshell particles (Gold-Silica Nanoshells). *Int. J. Toxicol* 2012, 31, 584–594. [PubMed: 23212452]

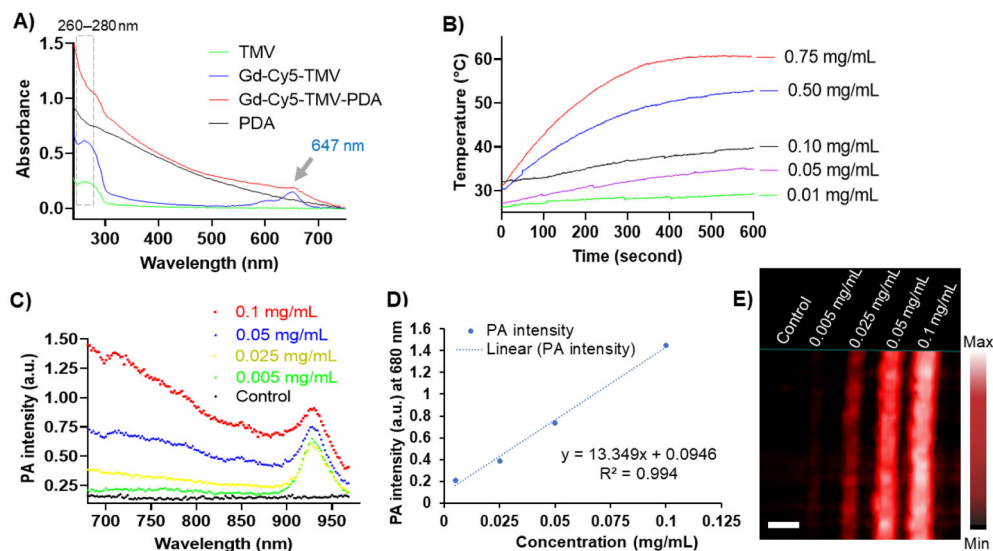
75. Liu Z, Davis C, Cai W, He L, Chen X, & Dai H Circulation and long-term fate of functionalized, biocompatible single-walled carbon nanotubes in mice probed by Raman spectroscopy. *Proc. Natl. Acad. Sci. U. S. A* 2008, 105, 1410–1415. [PubMed: 18230737]
76. Liu X, Cao J, Li H, Li J, Jin Q, Ren K, & Ji J Mussel-inspired polydopamine: A biocompatible and ultrastable coating for nanoparticles in vivo. *ACS Nano* 2013, 7, 9384–9395. [PubMed: 24010584]
77. Bettinger CJ, Bruggeman JP, Misra A, Borenstein JT & Langer R Biocompatibility of biodegradable semiconducting melanin films for nerve tissue engineering. *Biomaterials* 2009, 30, 3050–3057. [PubMed: 19286252]





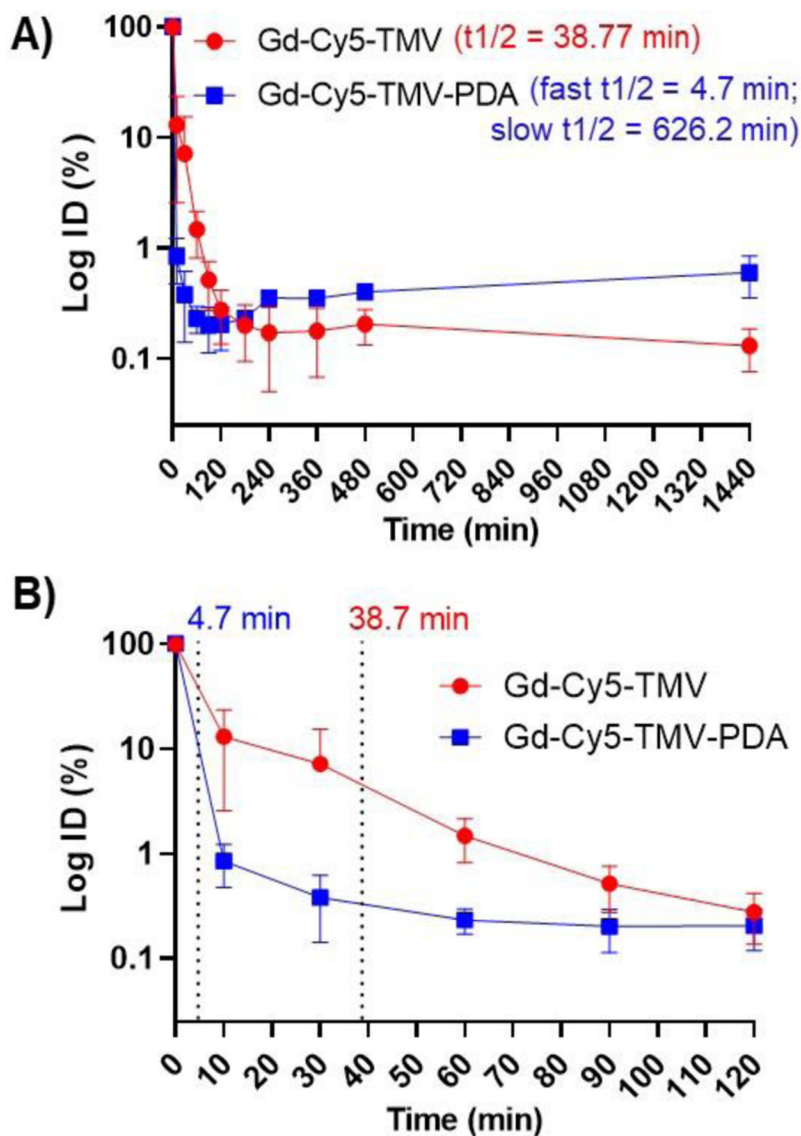
**Figure 1.**

Characterization of the TMV-based particles. **A)** Size exclusion chromatography showing similar elution profiles at 260 nm (protein) and 280 nm (RNA) for TMV, and the same for Gd-Cy5-TMV as well at 647 nm (sulfo-Cy5). **B)** TEM showing the smooth surface of the uncoated particles compared to the rough surface of the coated particles. The black scale bar is 200 nm. **C)** SDS-PAGE analysis under white light, after staining with Coomassie Brilliant Blue, and under red light to detect Cy5. The contents of each lane are listed in the figure panel.

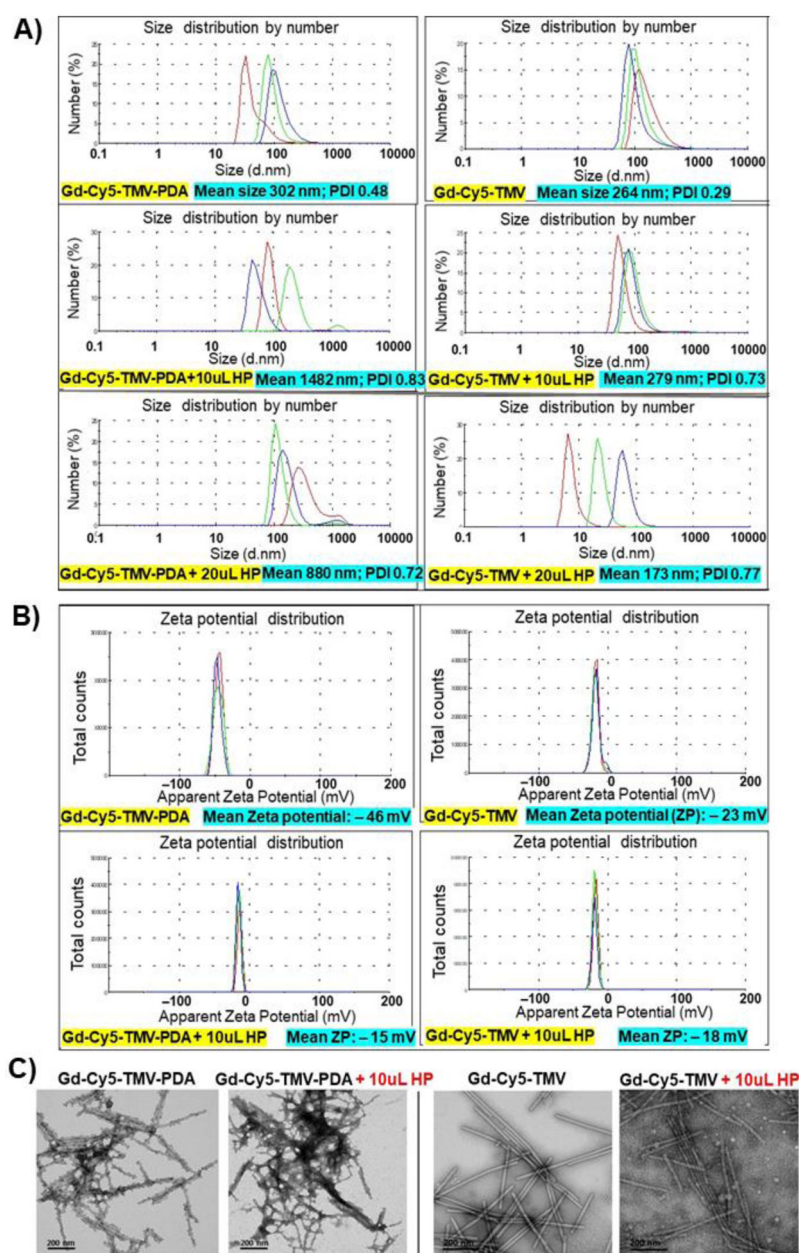


**Figure 2.**

The optical properties of PDA-coated Gd-Cy5-TMV particles. **A)** UV-Vis absorption spectra: the dashed frame shows the spectral features of TMV (coat protein and RNA) whereas the arrow indicates the overlapping Cy5 dye signals from coated vs. uncoated particles. **B)** The changing temperature profile of Gd-Cy5-TMV-PDA solutions during irradiation with an 808-nm laser at  $1 \text{ W/cm}^2$ . **C)** Photoacoustic spectra of Gd-Cy5-TMV-PDA at different concentrations over the wavelength range 680–970 nm. **D)** Calibration graph showing the correlation between Gd-Cy5-TMV-PDA concentrations and the corresponding photoacoustic signal intensities. **E)** Photoacoustic imaging phantoms of the solutions irradiated at 680 nm. The white scale bar is 2 mm.

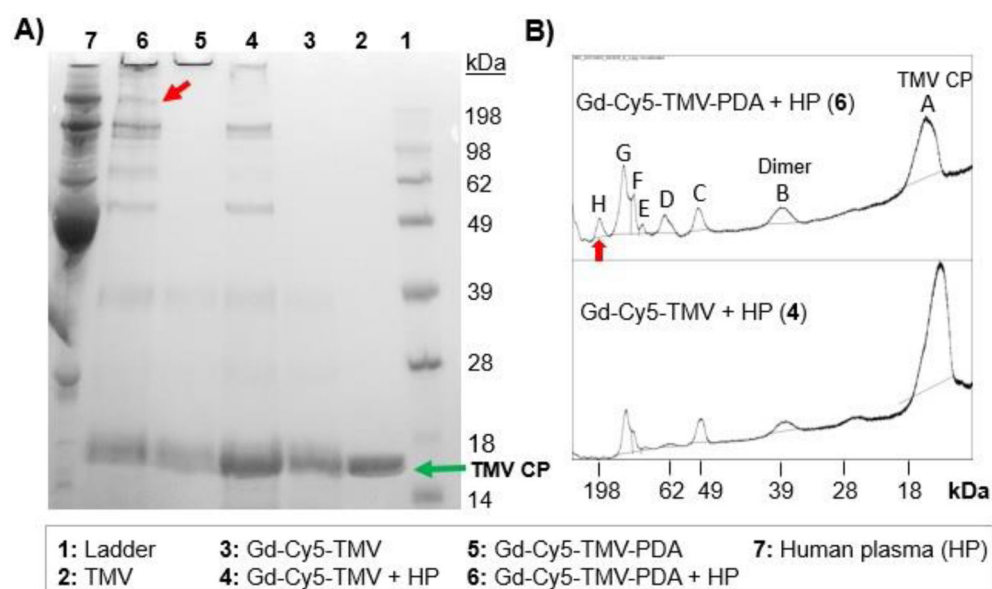


**Figure 3.** Pharmacokinetics (PK) of Gd-Cy5-TMV and Gd-Cy5-TMV-PDA in female BALB/c mice. Particles were administered by tail vein injection (200  $\mu$ g/mouse,  $n = 3$ ) and blood samples were taken by retro-orbital bleeding at 0, 10, 30, 60, 90, 120, 240, 360, 480 and 1440 min post-injection for Gd<sup>3+</sup> analysis by ICP-OES. The ID% values were then used to calculate the plasma circulation half-life. **A)** Full PK data showing logarithmic scale of percent injected dose (ID%) over all time points (1440 mins). **B)** PK data excerpt showing logarithmic ID% over early time points (120 mins). ID% data are plotted using the log 10 scale.



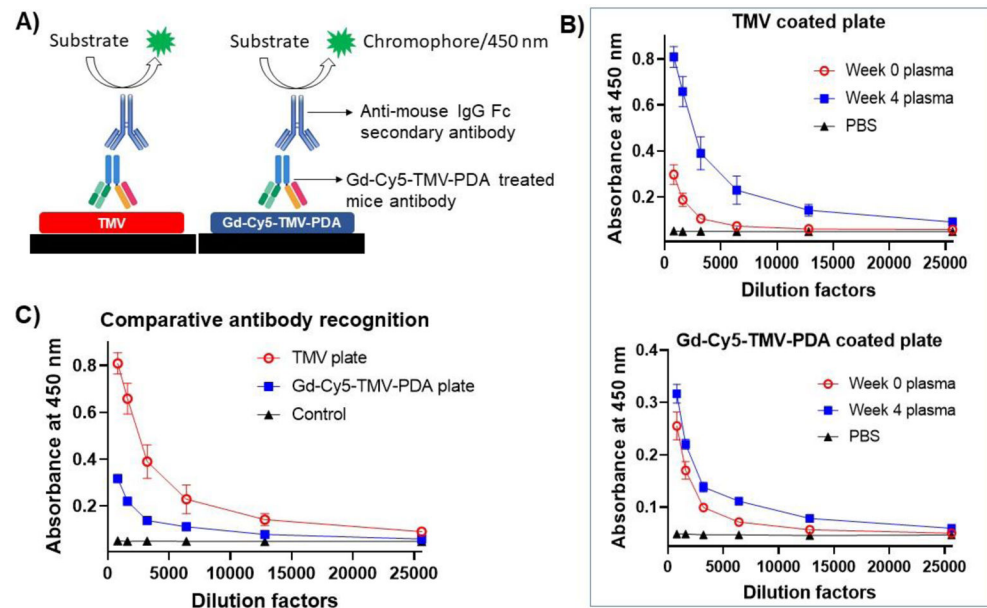
**Figure 4.**

Characterization of PDA-coated and uncoated Gd-Cy5-TMV particles before and after incubation for 1 h in human plasma (HP). **A)** DLS data from triplicate particle size measurements showing variation in hydrodynamic size distribution by percentage due to protein corona formation on PDA-coated particles. **B)** Triplicate measurements of zeta potential (ZP) showing variation in net surface charge due to the adsorption of plasma proteins on PDA-coated particles. **C)** TEM images showing protein corona-induced agglomeration of PDA-coated particles. The black scale bar is 200 nm.



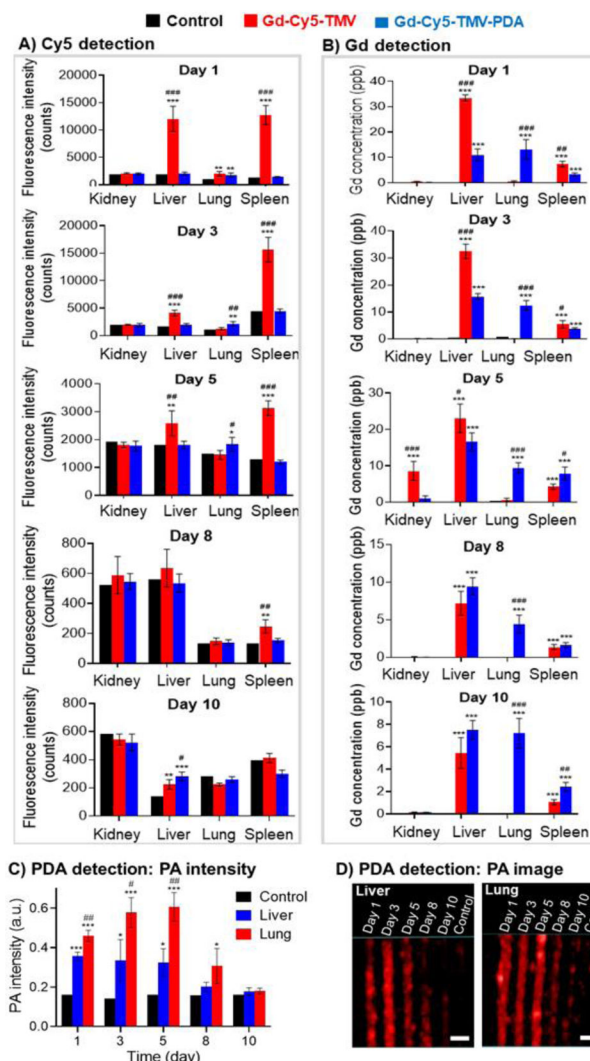
**Figure 5.**

Hard corona protein profiles of PDA-coated and uncoated Gd-Cy5-TMV particles after extensive washing following incubation in human plasma for 1 h. **A)** SDS-PAGE analysis of protein corona shows additional bands on the coated particles. **B)** Densitometric analysis of the bands from the main SDS-PAGE lanes in panel **A**, showing quantitative differences in the corona proteins. The red arrow indicates the corona protein band that distinguishes Gd-Cy5-TMV-PDA from Gd-Cy5-TMV.



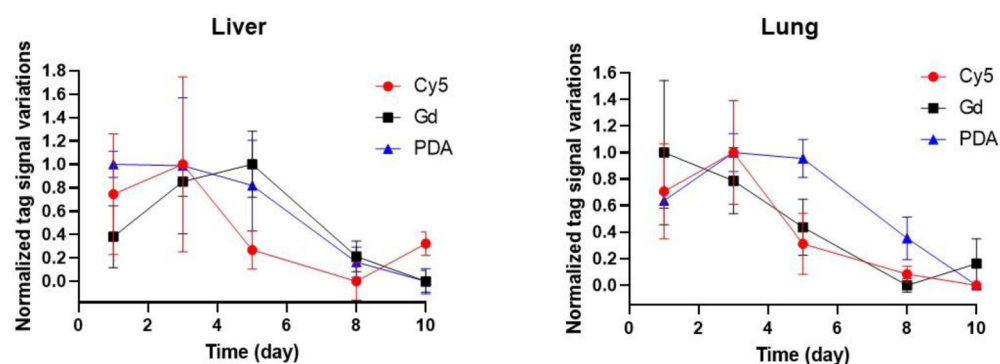
**Figure 6.** Production and recognition of TMV-specific antibodies. **A)** Schematic representation of ELISA experiments. **B)** Comparison of TMV antibody levels before (week 0) and 4 weeks after the administration of Gd-Cy5-TMV-PDA (200  $\mu$ g per female BALB/c mouse,  $n = 3$ ), confirming the elicitation of antibodies. **C)** The recognition of wild-type TMV and Gd-Cy5-TMV-PDA by TMV-specific antibodies, indicating the less efficient binding of the antibodies to PDA-coated particles.





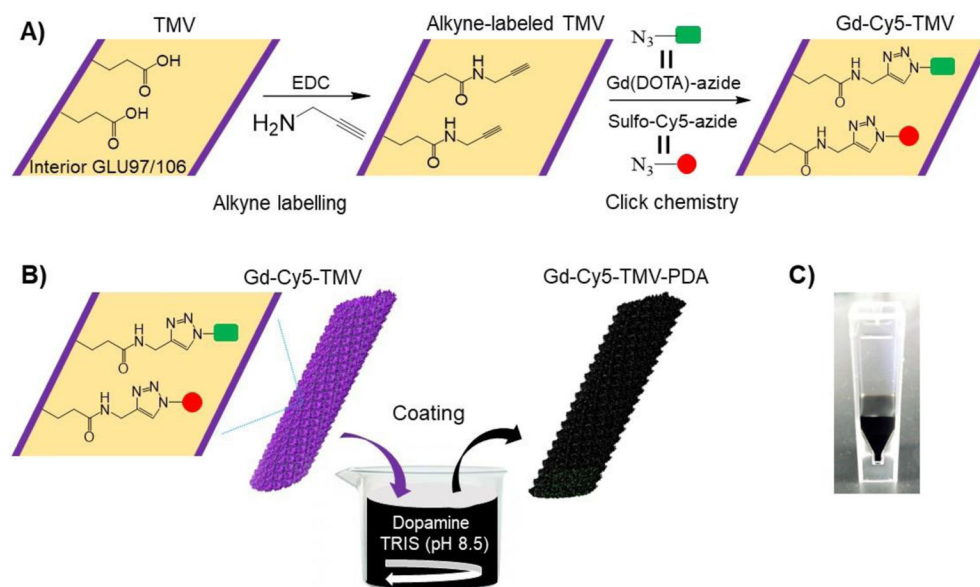
**Figure 7.**

Quantitative analysis of the distribution and clearance of Gd-Cy5-TMV and Gd-Cy5-TMV-PDA at different time points following the retro-orbital injection of female BALB/c mice (dose = 200  $\mu$ g, n = 5). **A)** Cy5 fluorescence intensity based on IVIS imaging of harvested organs. **B)** Gd concentrations based on ICP-OES analysis of organs digested in hot nitric acid. **C)** Photoacoustic signal intensity (680 nm) in homogenized organs from Gd-Cy5-TMV-PDA mice (n = 3). **D)** Photoacoustic imaging phantoms (680 nm) for homogenized liver and lungs from Gd-Cy5-TMV-PDA mice. The white scale bar is 2 mm. \*Significant differences compared to control (\* $p$  < 0.05; \*\* $p$  < 0.01; \*\*\* $p$  < 0.001). #Significant differences between study groups (# $p$  < 0.05; ## $p$  < 0.01; ### $p$  < 0.001).



**Figure 8.**

Variations in the signals from three different tags (Cy5 fluorescence,  $\text{Gd}^{3+}$  concentration and PDA photoacoustic intensity). Control signals were subtracted and the data normalized in fractions. The co-localization (tag signal  $> 0$ ) of the three tags up to day 8 suggests the presence of intact Gd-Cy5-TMV-PDA particles, whereas the isolated Cy5 and Gd signals on day 10 suggest the particles are starting to break down and release the different tags.

**Scheme 1.**

Synthesis of Gd-Cy5-TMV-PDA particles: **A)** Dual decoration of internal glutamate residues with Gd-complexes and sulfo-Cy5 dye molecules. **B)** Coating the internally labeled TMV with polydopamine (PDA) by the oxidative polymerization of dopamine under alkaline conditions. Structures were drawn using ChemDraw Professional v15.0. TMV structural images were created using UCSF Chimera 1.15 (PDB ID: 2TMV). **C)** A picture of quartz cuvette containing  $0.5 \text{ mg mL}^{-1}$  solution of Gd-Cy5-TMV-PDA.

**Table 1.**

The densitometric quantitation of SDS-PAGE bands representing Gd-Cy5-TMV-PDA hard corona proteins in conjunction with the TMV coat protein. Bands are designated according to Figure 5B.

| Corona protein band | Band area ratio of corona protein to CP |              |
|---------------------|---|--------------|
|                     | Gd-Cy5-TMV-PDA                          | Gd-Cy5-TMV   |
| C                   | 0.222                                   | 0.071        |
| D                   | 0.161                                   | 0.083        |
| E                   | 0.123                                   | 0.011        |
| F                   | 0.145                                   | 0.033        |
| G                   | 0.472                                   | 0.128        |
| H                   | 0.101                                   | Not detected |

**Table 2.**

The most abundant proteins identified in the Gd-Cy5-TMV-PDA hard corona after incubation with human plasma and extensive washing.

| Bands from SDS-PAGE<br>Band ID* (Molecular<br>weight in Da) | Protein name   | Protein accession number | Protein molecular<br>weight (Da) | Total spectrum<br>count |
|---|--|--------------------------|----------------------------------|-------------------------|
| <b>A (~18,000)</b>  | Capsid protein (CP) of TMV (strain U1)                     | P69687 (CAPSD_TMV)       | 17,624                           | 454                     |
|   | Capsid protein (CP) of TMV (strain U1)                     | P69687 (CAPSD_TMV)       | 17,624                           | 134                     |
|   | Capsid protein (CP) of TMV (strain U1)                     | P69687 (CAPSD_TMV)       | 17,624                           | 67                      |
| <b>B (~40,00)</b>   | Albumin isoform 2, <i>Homo sapiens</i>                     | P02768-2 (ALBU_HUMAN)    | 47,360                           | 153                     |
|   | Immunoglobulin gamma-1 heavy chain, <i>Homo sapiens</i>    | P0DOX5 (IGG1_HUMAN)      | 49,329                           | 63                      |
|   | Capsid protein (CP) of TMV (strain U1)                     | P69687 (CAPSD_TMV)       | 17,624                           | 778                     |
| <b>D (~65,000)</b>  | Albumin isoform 1, <i>Homo sapiens</i>                     | P02768-1 (ALBU_HUMAN)    | 69,367                           | 392                     |
|   | Plasminogen, <i>Homo sapiens</i>                           | P00747 (PLMN_HUMAN)      | 90,569                           | 42                      |
|   | Albumin isoform 1, <i>Homo sapiens</i>                     | P02768-1 (ALBU_HUMAN)    | 69,367                           | 60                      |
| <b>E (~90,000)</b>  | Gelsolin, <i>Homo sapiens</i>                              | P06396 (GELS_HUMAN)      | 85,698                           | 23                      |
|   | Junction plakoglobin, <i>Homo sapiens</i>                  | P14923 (PLAK_HUMAN)      | 81,745                           | 30                      |
|   | Capsid protein (CP) of TMV (strain U1)                     | P69687 (CAPSD_TMV)       | 17,624                           | 72                      |
| <b>F (~180,000)</b>   | Complement C4-A, <i>Homo sapiens</i>                       | P0C0L4 (CO4A_HUMAN)      | 192,785                          | 47                      |
|   | Complement C4-B, <i>Homo sapiens</i>                       | P0C0L5 (CO4B_HUMAN)      | 192,751                          | 47                      |
|   | Complement factor H, <i>Homo sapiens</i>                   | P08603 (CFAH_HUMAN)      | 139,096                          | 523                     |
| <b>G (~190,000)</b>   | Immunoglobulin heavy constant gamma 1, <i>Homo sapiens</i> | P01857 (IGHG1_HUMAN)     | 36,106                           | 782                     |
|   | Immunoglobulin heavy constant gamma 2, <i>Homo sapiens</i> | P01859 (IGHG2_HUMAN)     | 35,901                           | 778                     |
|   | Immunoglobulin heavy constant gamma 3, <i>Homo sapiens</i> | P01860 (IGHG3_HUMAN)     | 41,287                           | 61                      |
| <b>G (~190,000)</b>   | Immunoglobulin heavy constant gamma 4, <i>Homo sapiens</i> | P01861 (IGHG4_HUMAN)     | 35,941                           | 772                     |
|   | Fibrinogen alpha chain, <i>Homo sapiens</i>                | P02671 (FIBA_HUMAN)      | 94,973                           | 94                      |
|   | Complement C3, <i>Homo sapiens</i>                         | P01024 (CO3_HUMAN)       | 187,148                          | 38                      |
| <b>G (~190,000)</b>   | Immunoglobulin lambda constant 2, <i>Homo sapiens</i>      | P0DOY2 (IGLC2_HUMAN)     | 11,294                           | 34                      |
|   | Immunoglobulin lambda constant 3, <i>Homo sapiens</i>      | P0DOY3 (IGLC3_HUMAN)     | 11,266                           | 34                      |
|   | Immunoglobulin lambda constant 6, <i>Homo sapiens</i>      | P0CF74 (IGLC6_HUMAN)     | 11,277                           | 34                      |
| <b>G (~190,000)</b>   | Immunoglobulin lambda constant 7, <i>Homo sapiens</i>      | A0M8Q6 (IGLC7_HUMAN)     | 11,254                           | 34                      |

| Bands from SDS-PAGE<br>Band ID* (Molecular<br>weight in Da)    | Protein name  | Protein accession number | Protein molecular<br>weight (Da) | Total spectrum<br>count |
|--|---|--------------------------|----------------------------------|-------------------------|
| <b>H (~198,000)<br/>(missing in the lane of Gd-Cy5-TMV+HP)</b> | Capsid protein (CP) of TMV (strain U1)                | P69687 (CAPSD_TMV)       | 17,624                           | 587                     |
|  | Immunoglobulin kappa constant, <i>Homo sapiens</i>    | P01834 (IGKC_HUMAN)      | 11,765                           | 604                     |
|  | Immunoglobulin kappa light chain, <i>Homo sapiens</i> | P0DOX7 (IGK_HUMAN)       | 23,379                           | 604                     |
|  | Tyrosine-protein kinase ABL1, <i>Homo sapiens</i>     | P00519 (ABL1_HUMAN)      | 122,873                          | 13                      |

\* Band ID as indicated in Figure 5B